arXiv:1011.0090v1 [cond-mat.mtrl-sci] 30 Oct 2010

Large-amplitude chirped coherent phonons in tellurium mediated by ultrafast photoexcited carrier diffusion

N. Kamaraju, Sunil Kumar, M. Anija and A. K. Sood *

Department of Physics and Center for Ultrafast Laser Applications (CULA), Indian Institute of Science, Bangalore - 560 012, India

(Dated: February 15, 2022)

Abstract

We report femtosecond time-resolved reflectivity measurements of coherent phonons in tellurium performed over a wide range of temperatures (3K to 296K) and pump laser intensities. A totally symmetric A_1 coherent phonon at 3.6 THz responsible for the oscillations in the reflectivity data is observed to be strongly positively chirped (i.e, phonon time period decreases at longer pump-probe delay times) with increasing photoexcited carrier density, more so at lower temperatures. We show for the first time that the temperature dependence of the coherent phonon frequency is anomalous (i.e, increasing with increasing temperature) at high photoexcited carrier density due to electron-phonon interaction. At the highest photoexcited carrier density of $\sim 1.4 \times 10^{21}\text{cm}^{-3}$ and the sample temperature of 3K, the lattice displacement of the coherent phonon mode is estimated to be as high as ~ 0.24 Å. Numerical simulations based on coupled effects of optical absorption and carrier diffusion reveal that the diffusion of carriers dominates the non-oscillatory electronic part of the time-resolved reflectivity. Finally, using the pump-probe experiments at low carrier density of 6×10^{18} cm^{-3}, we separate the phonon anharmonicity to obtain the electron-phonon coupling contribution to the phonon frequency and linewidth.

PACS numbers:

* Electronic mail: asood@physics.iisc.ernet.in

I. INTRODUCTION

The investigation of ultrafast carrier and phonon dynamics in semiconductors is of special interest as their applications in information technology depends on the understanding of fundamental processes like momentum and energy relaxation, as well as mechanisms such as carrier-carrier scattering, inter-valley and intra-valley scattering, optical phonon scattering, and carrier diffusion [1]. When a semiconductor is irradiated with an ultrashort laser pulse with photon energy much higher than the band gap, it excites electrons from valence band to the conduction band with excess of energy above the bottom of the conduction band. The carrier distribution immediately after the photoexcitation is of non-Fermi-Dirac type (non-thermal) [2] where the temperature of the excited carriers is still not defined. Subsequently the carrier-carrier interactions lead to a formation of Fermi-Dirac distribution with a definite electron temperature (also called as thermalization of carriers) from the initial nonthermal state and this process depends on the excited carrier density. At moderate carrier density of $\sim 10^{18}$ cm^{-3}, this carrier-carrier interaction time is ~ 200 fs in GaAs [2, 3] which can reduce to a few fs at higher photoexcited carrier densities. Following this, the hot carriers diffuse in the material as well as emit phonons. The magnitude of cooling time again depends on the number of excited carriers and the initial temperature of the distribution. Typically, carrier cooling times are of the order of a few picoseconds in semiconductors [4]. There is, finally, the electron-hole recombination which happens on the time scale of several picoseconds to nanoseconds.

In recent years, the femtosecond pulses have been used to generate and probe coherent phonons in solids [5–9]. The excitation mechanism of coherent phonons was thought to be impulsive stimulated Raman scattering (ISRS) [5] in transparent materials whereas displacive excitation of coherent phonons (DECP) is the dominant mechanism in opaque samples [6–8]. Later, it was shown that DECP is a special case of ISRS when excited resonantly [9]. In a resonant ISRS/DECP process, the photo-excitation of electrons changes the equilibrium positions of the atoms; the atoms then oscillate around their new equilibrium positions. In absorbing samples like Te, the Dember field arising from different diffusion coefficients of photo-excited electrons and holes can also contribute to the generation of coherent phonons [10–12].

Till now, there have been only a very few ultrafast coherent phonon studies at photoex-

cited carrier densities (PCD) as high as 10^{20} cm^{-3} [13–19]. A red shift of frequency of the totally symmetric A_1 phonon was observed in a narrow band gap semiconductor, tellurium, as the femtosecond laser injected carrier density was increased to 5×10^{21} cm^{-3} at room temperature in a degenerate pump probe reflectivity experiments [13, 14]. This was attributed to the bond weakening by the carriers [20]. In addition, the phonon time period was found to decrease with increase in the delay time between pump and probe pulses, leading to asymmetric line-shape in frequency domain [13]. This linear sweep in the frequency with the pump-probe time delay can be termed as phonon chirping which originates from the rapid change of photoexcited carrier density in the penetration depth of the sample due to carrier diffusion and its interaction with the coherent phonons. Similar phonon chirping has been seen in degenerate pump probe experiments on bismuth [17, 18] with PCD of $\geq 3 \times 10^{21}$cm^{-3}. Two pump pulse experiments [13, 19] along with first principal density functional calculations [15, 19] have established that the chirping arises from varying carrier density along the probed length in the sample and not due to lattice anharmonic effects.

We note here that all the previous studies on tellurium have been performed at room temperature. Here, we present femtosecond time-resolved reflectivity measurements of coherent phonon dynamics in tellurium performed over a wide range of temperatures (3K to 296K) and carrier density levels. The non-oscillatory part of the data associated with the strength of photoexcited carrier density is found to be dominated by diffusion of the carriers as revealed by our numerical simulations. The oscillatory part shows highly positively chirped A_1 phonons excited at photoexcited carrier density of $\sim 1.4 \times 10^{21}$ cm^{-3} and the chirping is found to be largest at lower temperatures where the carrier diffusion time and the strength of photoexcited carrier density were found to be maximum. Apart from the phonon chirping, the associated lattice displacement is estimated to be as high as ~ 0.24 Å at 3K. The other important result is the observation of increased softening of A_1 mode with the pump fluence at 3K (-0.16 THz/mJ-cm^{-2}) as compared to 296K (-0.08 THz/mJ-cm^{-2}) consistent with the increased photoexcited carriers at lower temperatures. Using time-resolved reflectivity experiments performed at low carrier density levels of $\sim 6 \times 10^{18}$ cm^{-3} where phonon chirping is found to be absent, the effects of phonon anharmonicity and high carrier density are separated and analysed.

II. SAMPLE DETAILS

In our experiments, we have used a polycrystalline tellurium crystal ($6\times4\times2$ mm^3) mounted on a continuous helium flow optical cryostat. Tellurium is a narrow band semiconductor with a band gap of ~ 0.33 eV [15]. It crystallizes into $P3_121$ structure with the point group D_3^4 and three atom basis arranged around a screw axis parallel to the c axis of the hexagonal unit cell forming a helical structure. The equilibrium lattice constants are $a = 4.456$ Å (distance between two helices) and $c = 5.927$ Å. The interatomic spacing in a chain is 2.834 Å and the helical radius is $u = 1.173$ Å. Group theory gives the allowed Raman modes [21] as A_1 (~ 3.6 THz)+ E^1_{TO}(~ 2.8 THz) + E^2_{TO}(~ 4.2 THz). The totally symmetric A_1 mode corresponds to symmetric inter-chain dilation and compression normal to the chain axis, involving bond length and bond angle distortions. In this mode, a and c do not change whereas only helical radius u changes.

The linear absorption coefficient [22], α, of Te at 1.57 eV is 2×10^5 cm^{-1} which gives the penetration depth ξ ($\sim 1/\alpha$) of pump light to be ~ 50 nm. At maximum pump fluence of 3.3 mJ/cm^2, the excited carrier density is $N_0 = F\alpha(1-R)/E_p$ is $\sim 1.4\times10^{21}$ cm^{-3} which is 0.8 % of the total density of electrons in the valence band. Here, F is the pump fluence in J/cm^2, R is the reflectivity (0.46 at 1.57 eV) of tellurium and E_p is the photon energy in J.

III. EXPERIMENTAL DETAILS

Degenerate femtosecond pump-probe experiments in the reflection geometry were carried out using femtosecond pulses derived from Ti:Sapphire amplifier producing 50 fs pulses with the central photon energy of 1.57 eV at a repetition rate of 1 kHz. The pump beam was modulated at 393 Hz with a mechanical chopper and the reflected probe intensity was recorded with a Si-PIN diode and a lock-in amplifier. The pulse width at the sample point was 65 fs (FWHM) measured using a thin beta-barium borate (BBO) crystal. The spot sizes (half width at 1/e maximum) of the pump and the probe beams were kept at 600 μm and 400 μm, respectively at the overlap of the two beams at the sample. The difference between the probe intensity reflected from the sample and that of a reference beam was recorded as a function of delay between the pump and probe pulses. Both the pump and probe beams were kept close to the normal incidence with their polarizations perpendicular

to each other. This detection scheme can detect only A_1 mode for a single crystal. However, the non-symmetric E modes can be seen as well for a polycrystalline sample with major crystal axes oriented at an angle from the surface [11, 17]. In our experiments, we observed that the damage threshold is $\sim$ 4.5 mJ/cm^2 which is much smaller than the value of 12 mJ/cm^2 reported earlier [13]. The pump fluence was varied between 3.3 mJ/cm^2 and 0.3 mJ/cm^2 whereas the probe fluence was kept at 0.04 mJ/cm^2. The time-resolved reflectivity was recorded at four temperatures - 3K, 80K, 160K and 296K. At the lowest pump fluence of 14 μJ/cm^2 (probe fluence $\sim$ 0.8 μj/cm^2), the transient reflectivity data was recorded as a function of temperature from 296K to 3K using femtosecond pulses derived from the oscillator (50fs, Tsunami, 76MHz, Spectra Physics Inc) in the fast scan scheme [23]. In this scheme the pump delay line is modulated with a shaker at 65 Hz and the time-resolved signal was detected with a fast A/D converter (AIXscan data acquisition system, AMO GmbH, Germany Inc.) which helps in capturing relative signal changes of $\sim 10^{-7}$ without using a lock-in amplifier [23].

IV. RESULTS AND DISCUSSION

The summary of results at 3K for various pump fluences is presented in Fig.1 where the panel (a) is for the time domain data and panel (b) shows the Fast Fourier Transform (FFT) of the oscillatory part of the data. The signal contains damped oscillations associated with the generated coherent phonons overlaid on an exponentially decaying background. This background can be assigned to direct changes in electronic susceptibility by the photoexcited carriers [13]. The vertical dashed line in frequency domain is a guide to the eye to appreciate the red shift of the peak frequency with increased pump fluence. The time domain data at the lowest pump fluence of 0.25 mJ/cm^2 can be fitted with the following equation

$$\frac{\Delta R}{R} = y_0 + A_{el}\, \exp(-t/\tau_{el}) + B\, \exp(-t/\tau)\, cos(2\pi\nu t + \phi) \qquad (1)$$

where τ_{el} is electronic relaxation time; and $A_{el} \equiv (\frac{\Delta R}{R})_{el}$ is the strength of electronic relaxation contributions; $B \equiv (\frac{\Delta R}{R})_{ph}$, τ, ν, and ϕ denote the amplitude, relaxation time, frequency, and initial phase of the coherent phonon oscillations, respectively. Here y_0 denotes the background arising from long relaxation time constant (>1 ns) which may be associated with slow electron-hole recombination time. At higher pump intensities, the fit

to the data using Eq. (1) was found to be unsatisfactory as the frequency rendering a good fit at short time delays deviates considerably from the data at longer time delays. This is demonstrated in Fig. 2 (a) and (b) for the time domain reflectivity data and FFT of its oscillatory part at 3K and pump fluence of 3.3 mJ/cm^2 where thin grey line is the fit using Eq. (1). The experimental data is best fitted by taking into account of phonon chirping. The transient reflectivity data is modelled as

$$\frac{\Delta R}{R} = y_0 + A_{el}\ \exp(-t/\tau_{el}) + \sum_{i=1,2,3} B_i\ \exp(-t/\tau_i)\ cos(2\pi\nu_i t + \beta_i t^2 + \phi_i) \qquad (2)$$

where β is the chirp parameter describing linear sweep in the phonon frequency with the pump-probe delay time. Here the fit is carried out with three modes (represented by subscript, $i = 1, 2$ and 3) guided by the FFT (Fig. 2 (b)). The coherent phonon modes observed at 2.45 THz, 3.25 THz and 4.13 THz are attributed to E^1_{TO}, A_1 and E^2_{TO}, respectively. It is found that the Eq. (2) furnishes a very good fit (black line in Fig. 2(a) and 2(b)) to the data. The chirping is significant for only the A_1 mode ($i = 2$) for which the obtained fitting parameters are $\beta_2 = 0.55$ ps^{-2}, $\nu_2 = 3.24$ THz, $\tau_2 = 0.81$ ps and $B_2 = 0.22$. The value of A_1 phonon oscillation amplitude, B_2 is 34% of the maximum change in reflectivity, $(\frac{\Delta R}{R})_{max}$($= 0.648$). We note that the non-symmetric E-modes were observed only at 3K using pump-fluence of 3.3 mJ/cm^2. For pump fluences lesser than 3.3 mJ/cm^2, data are fitted using Eq. (2) by taking only one coherent phonon (A_1). The fits as shown in time and frequency domain in Fig. 1 are excellent.

The lattice displacement of the coherent phonon modes can be estimated for absorbing materials like bismuth from [16, 24]

$$U_i^2 \sim \frac{3.8 \times 10^{-3}\ B_i\ F}{\varrho \nu_i |\varepsilon|} \left[\frac{(\frac{2\varepsilon_2}{E_{ph}})}{D}\right] \qquad (3)$$

where U_i is in Angstrom (Å), F is the pump fluence in mJ/cm^2, ϱ is the density of the material in amu/Å^3 and ε is the dielectric constant ($\varepsilon = \varepsilon_1 + j\varepsilon_2$), E_{ph} is the energy of the phonon in eV and $D = \frac{1}{R}\frac{\partial R}{\partial E}$ with E as the photon energy in eV. Now, for Te at 1.57 eV, $D = \frac{1}{R}\frac{\partial R}{\partial E} \sim 10^{-1} eV^{-1}$, $\left(\frac{2\varepsilon_2}{E_{ph}}\right) \sim 10^3 eV^{-1}$, and $\varepsilon = 32 + j11$ ($|\varepsilon| = 34$) at 300K [22]. The value of $|\varepsilon|$ at 10K is 27 [22]. Since the exact temperature dependence of $|\varepsilon|$ is not available, we have used $|\varepsilon| = 34$ at all temperatures. This will introduce a maximum error of $\sim 10\%$

at 10K. The final expression for the lattice displacement in this case is

$$\mathrm{U}_i \sim \sqrt{B_i \frac{38\ F}{\varrho \nu_i |\varepsilon|}} \tag{4}$$

This gives a very high value of $\mathrm{U}_2 \sim 0.24$ Å which is almost twice of ~ 0.13 $\mathring{A}$ estimated in Bi [17]. In terms of the lattice constant $a = 4.4561$ Å, $\mathrm{U}_2 \sim 0.05a$ which is unusually very high. The oscillation amplitude of E^1_{TO} and E^2_{TO} are, B_1= 0.03 and B_3= 0.01 respectively corresponding to lattice displacements of $\mathrm{U}_1 \sim 0.11$ Å and $\mathrm{U}_3 \sim 0.05$ Å. Thus the huge lattice displacements caused by the high carrier density excitation may be responsible for observing the forbidden E_{TO} modes in isotropic reflectivity detection scheme [17]. The possibility of these E modes due to major crystal orientation in the polycrystalline sample is perhaps negligible as these modes were seen only at 3K with the highest pump-fluence. Since E-modes are absent at all lower pump fluences and temperatures higher than 3K, we proceed now to discuss only the A_1 mode's behavior. From here, we make a change in notation for the fit parameters corresponding to phonons as, B_{ph}, τ_{ph}, ν_{ph}, β and ϕ. The fit parameters of the non-oscillatory electronic part and the oscillatory phononic part are presented in the following sections.

A. Electronic part

Fig. 2(c) and 2(d) show the dependence of A_{el} and τ_{el} on PCD at four different temperatures. It is seen from Fig. 2(c) that the strength of the electronic contribution, A_{el} increases with the pump fluence at all temperatures. A_{el} is fitted (solid line in the figure) with $\mathrm{A}_{el} \sim N^p$ where $p = 1.5$ at 3K and 80K; and $p = 1.0$ at 160K and 296K. The photoexcited carrier relaxation time, τ_{el} increases with the PCD (N) (Fig. 2(d)) and saturates at $\sim 0.6 \times 10^{21}$ cm^{-3}. Figs. 2(e) and 2(f) display A_{el} and τ_{el} *vs* temperature at different PCD (legend C1-C5 corresponds to 0.1, 0.2, 0.4, 0.6 and 1.4×10^{21} cm^{-3}). Thick lines in Fig. 2 (e) are the linear fits ($\mathrm{A}_{el}(\mathrm{T}) = \mathrm{A}_{el}(0)$- bT). It is seen from Fig. 2(e) that A_{el} increases with lowering of the sample temperature, reaching a maximum value of 0.36 at 3K (at 1.4×10^{21} cm^{-3}), almost 4 times higher than its value at 296K. The trend is same at other PCDs. We do not yet understand the temperature and PCD dependences of A_{el}. The dependence of τ_{el} (Fig. 2(f)) on temperature is rather anomalous: the electron relaxation time is seen to increase with increase in temperature. The solid lines in Fig. 2 (d) and (f) are drawn as guide to the

eye.

We now try to understand carrier dynamics using the diffusion of photoexcited carriers with time. When a femtosecond pump pulse irradiates the sample, it creates a carrier density, N_0 on the surface depending on the absorption coefficient and the fluence. The carrier diffusion leads to a rapid decay of these carriers across the surface. The diffusion coefficients of photo-generated electrons and holes can be different leading to a Dember field [10–12] with a build up time of 100 fs to 200 fs after the pump excitation. Since the carrier relaxation times in our experiments are long (2 ps to 6 ps as shown in Fig. 2(d)), we work with the assumption of ambipolar diffusion of carriers, described by the diffusion equation [26]

$$\frac{\partial N}{\partial t} = D_a \frac{\partial^2 N}{\partial z^2} + \frac{N_0}{\tau_p} e^{(-t/\tau_p)^2} e^{-z/\xi} \tag{5}$$

where τ_p is the pulse width, D_a is the ambipolar diffusion coefficient and z is the depth inside the medium. We solved this partial differential equation numerically for the carrier density N(z,t) with the initial condition $N(z,0) = N_0$ and the boundary conditions, $D_a \frac{\partial N}{\partial z}$=0 at $z = 0$ and and $N(L,t) = N_0\ \mathrm{e}^{-L/\xi}$. The phonon displacement, x_{ph}, given by a damped harmonic oscillator where the displacement and the angular frequency, $\Omega_0(N)$ depend on the carrier density $N(z,t)$ [15]

$$\frac{\partial^2 x_{ph}}{\partial t^2} + \Omega_0(N)^2[x_{ph} - x_0(N)] + \Gamma \frac{\partial x_{ph}}{\partial t} = 0 \tag{6}$$

Here Γ is a damping constant for the phonon. In linear approximation (which is expected to be valid since the PCD is less than 1% of the valence electron density), the carrier density dependence of phonon displacement, $x_0(N)$ and the angular frequency, $\Omega_0(N)$ are taken as, $x_0(N) = x_{eq} + (\partial x_0/\partial N)N$ and $\Omega_0(N) = \Omega_{eq} + (\partial \Omega_0/\partial N)N$; x_{eq} and Ω_{eq} are the lattice displacement and angular phonon frequency at equilibrium (at low carrier density levels). We have used $x_{eq} = 0.2686\ a$ (ref. [15]) and the experimentally relevent values (Ω_{eq}= 23 THz and $\Gamma = 0.56$ THz and $\left[\frac{\partial \Omega_0}{\partial N}\right] = 1.74 \times 10^{-21}$ THz-cm^3 at 160K [see inset of Fig. 4 (d)]). Eq. (6) was solved numerically using fourth order Runge-Kutta method with the integration step of 2 fs. The dielectric constant $\varepsilon = \varepsilon_1 + j\varepsilon_2$ depends on x_{ph} and $N(z,t)$. Since $\varepsilon_1 = 32$, much larger than ε_2 (= 11), the changes in ε_1 will dominate the change in

the reflectivity. Thus,

$$\frac{\Delta R}{R} \approx \varsigma \left[\frac{\Delta\varepsilon_1}{\varepsilon_1}\right] \tag{7}$$

$$\text{with } \frac{\Delta\varepsilon_1}{\varepsilon_1} = \frac{1}{\varepsilon_1}\left[\left(\frac{\partial\varepsilon_1}{\partial x_{ph}}\right) x_{ph} + \left(\frac{\partial\varepsilon_1}{\partial N}\right) N\right] \tag{8}$$

where $\frac{\partial\varepsilon_1}{\partial x_{ph}}$, $\frac{\partial\varepsilon_1}{\partial N}$ and ς are taken as adjustable parameters to fit the experimentally observed background and initial oscillations in the reflectivity. As an example, the data at 160K and the fit using the Eqs. (5)-(8) are shown in Fig. 3 in panel (A) for different values of pump fluence. The variation of ambipolar diffusivity, D_a extracted from the fit are used to calculate the diffusion time $\tau_d \sim \xi^2/D_a$. The panel (B) of Fig. 3 displays thus derived (shown by stars) τ_d *vs* N (Fig. 3 (a2)-(d2)) and τ_d *vs* T (Fig. 3 (e2)-(h2)). Thick lines are drawn as a guide to the eye and they are not due to digital smoothing. Comparison of Fig. 3 (a2)-(d2) with Fig. 2 (d) shows that the values of τ_d and τ_{el} are comparable and their dependence on N is similar. Similarly, it is seen that the behavior of τ_d *vs* T (Fig. 3 (e2)-(h2)) is compatible with τ_e *vs* T (Fig. 2 (f)) except at the lowest pump fluence. From the above analysis, it is clear that the carrier diffusion plays a major role in determining the reflectivity changes in tellurium after the the pump pulse excitation.

B. Phononic part

The dependence of phonon amplitude (B_{ph}) on pump fluence (Fig. 4 (a)) is similar to that of A_{el} (Fig.2 (c)). A plot of B_{ph} *vs* A_{el} given in the inset of Fig. 4 (a) shows a linear dependence between them, implying that the photoexcited carriers contribute mainly to the generation of coherent phonons as expected in a DECP process. The phonon lifetime, τ_{ph} decreases with increasing the pump fluence (see Fig. 4 (b)) due to electron-phonon interaction. Thick lines in (a) and (b) are the guide to the eye. At 3K, the phonon lifetime, τ_{ph} is $\sim$ 5.73 ps at the lowest PCD of $\sim 0.1 \times 10^{21}\text{cm}^{-3}$ (corresponding to the phonon linewidth $\gamma \equiv \frac{1}{\pi\tau_{ph}} = 0.056$ THz); this decreases by 87 % to 0.74 ps at the highest PCD of $1.4 \times 10^{21}\text{cm}^{-3}$. A similar behavior is seen at all other temperatures.

Next, we turn our attention to the chirp parameter β shown in Fig. 4 (c). The chirp parameter β is fitted (solid line) with $\sim N^\rho$ with $\rho = 2.2$ (3K), $\rho \sim 2.5$ (80K and 160K) and $\rho = 3.8$ (296K). The phonon chirping increases with increasing pump fluence; since $A_{el} \sim N^p$, $\beta \sim A_{el}^{\rho/p}$. It can be seen from Fig. 4 (c) that β increases on lowering the

temperature. For example, at highest PCD of 1.4×10^{21}cm^{-3}, $\beta \sim 0.55$ at 3K as compared to $\beta \sim 0.2$ at 296K.

We now look at the dependence of the observed phonon frequency as a function of photo carrier density at two temperatures, 3K and 296K as shown in Fig.4 (d). Here, the variation of the frequency is linear with N (linear fits are shown by solid lines in Fig. 4 (d)), as taken before in solving the Eq. (6). ν_{ph}(THz) = ν_0(THz)-y(THz cm^3) N(cm^{-3}) with ν_0 = 3.75 THz and 3.64 THz at 3K and 296K respectively; and $y \equiv \frac{1}{2\pi}\left[\frac{\partial\Omega_0}{\partial N}\right] = 3.73 \times 10^{-22}$ THz-cm^3 at 3K and 1.86×10^{-22} THz-cm^3 at 296K. The slope y determined here corresponds to the change in frequency with pump fluence as $\sim$ -0.16 THz/mJ-cm^{-2} (3K) and $\sim$ -0.08 THz/mJ-cm^{-2} (300K). The value at room temperature agrees well with the theoretically estimated value [15] of -0.085 THz/mJ-cm^{-2} at 296K for tellurium. The modulus of the slope, $|y|$ from this linear fit is plotted as a function of temperature in the inset of Fig. 4 (d) showing that the softening of phonons with carrier density decreases linearly with increasing temperature.

The lattice displacements of A_1 mode using Eq. (4) at various PCD *vs* temperatures are summarized in Fig. 4 (e) where the solid lines are connected through the data points as guide to the eye. Consistent with more photoexcited carriers at 3K (pump fluence of 3.3 mJ/cm^2), U/a is $\sim$ 5 %, which gradually decreases to 2.5 % at 296K, i.e a decrease by a factor of 2. The trend is similar for other pump fluences (see Fig. 4 (e)).

C. Low pump fluence experiments

To separate the effects of electron-phonon and phonon-phonon anharmonic interactions in the frequency and lifetime of coherent phonons presented above, we have performed the degenerate pump-probe reflectivity experiments with very low pump fluence of 14 μJ/cm^2 ($N_0 \sim 6 \times 10^{18}$ cm^{-3}). The varying non-oscillatory electronic background in the data is removed using FFT digital filter smoothing to extract the coherent phonon oscillations. Thus obtained data was fitted using Eq. (1) as the chirping is absent. The typical reflectivity data after FFT filtering at 3K along with the fit are shown in Fig 5 (a). The fitted parameters- the coherent phonon amplitude B_{ph}, damping parameter γ_{ph} ($\equiv \frac{1}{\pi\tau_{ph}}$) and the phonon frequency ν_{ph} are plotted as a function of temperature in Fig 5 (b), (c) and (d). It has been shown earlier [27] that the coherent phonon amplitude, B_{ph} behaves quite similar to Raman peak intensity

as $I_p \sim \frac{[n(\nu_{ph})+1]}{[2n(\nu_{ph}/2)+1]}$, where $n(\nu_{ph})$ is the BoseEinstein factor. The fit (solid line) using this expression is shown along with the data for B_{ph} in Fig. 5(b) where, B_{ph} is normalized with respect to its value at 3K. γ_{ph} and ν are fitted (solid line in Fig. 5 (c) and (d)) with the following well known functions [28, 29] based on cubic anharmonicity where the phonon of frequency ν decays into two phonons of equal frequency: $\gamma_{ph}(T) = \gamma_0 + \Delta\gamma_{anh}(T)$ with $\Delta\gamma_{anh}(T) = C[1 + 2n(\nu_0/2)]$ and $\nu_{ph}(T) = \nu_0 + \Delta\nu_{anh}(T)$ with $\Delta\nu_{anh}(T) = A[1 + 2n(\nu_0/2)]$ where ν_0, A, C and γ_0 are the fitting parameters (A and C are the measures of third order cubic anharmonicity). The parameters obtained from fitting are $\nu_0 = 3.70 \pm 0.01$ THz, A = -0.022 $\pm$ 0.002 THz, $\gamma_0 = 0.010 \pm 0.003$ THz and C = 0.042 $\pm$ 0.003 THz. Fig. 5(b), (c) and (d) show that the fits to the anharmonic contributions are excellent.

D. Electron-phonon coupling

In doped semiconductors, the electron-phonon interactions contribute to the linewidth (γ_i) of the i^{th} phonon of frequency ν_i and degeneracy g_i which is related to the dimensionless electron-phonon coupling constant λ_{EP} and density of states at the Fermi level (DOS(ϵ_F)) by the Allen's formula [30]: $\gamma_i = (2\pi/g_i)\lambda_{EP}\nu_i^2 DOS(E_F)$. The question arises what happens to phonons due to the photoexcited carriers under femtosecond pulse excitation. We address this question and extract the contribution of electron-phonon interaction to the phonon frequency and linewidth as described below.

The temperature dependance of ν_{ph} and γ_{ph} along with their linear fits at various pump fluences are drawn in Fig. 6 (a) and (b)(legends C1-C5 correspond to 0.1, 0.2, 0.4, 0.6 and 1.4 $\times$ 10^{21} cm^{-3}). We note that the effect of the carrier diffusion is explicitly taken into account while extracting the phonon parameters, ν_{ph} and γ_{ph} (shown in Fig. 6 (a) and 6 (b)) by fitting the total $\frac{\Delta R}{R}$ with Eq. 2. It can be seen that the normal anharmonic behavior of phonons (i.e, frequency increasing with lowering temperatures) at the lowest pump fluence of 0.1 $\times$ 10^{21} cm^{-3} changes gradually to an anomalous behavior (frequency decreasing with lowering temperatures) as the pump fluence is increased, suggesting a strong electron-phonon coupling at higher carrier densities. No such anomalous behavior is noticed in the phonon damping term (Fig. 6 (b)). The phonon frequency $\nu_{ph}(T)$ and damping $\gamma_{ph}(T)$ thus deduced have contributions both from electron-phonon and phonon-phonon anharmonic interactions. The temperature variation of frequency and linewidth of a phonon mode can be thus written

as [28, 31]

$$\nu_{ph}(T) = \nu_0 + \Delta\nu_{anh}(T) + \Delta\nu_{el-ph}(T) \quad (9)$$

$$\gamma_{ph}(T) = \gamma_0 + \Delta\gamma_{anh}(T) + \Delta\gamma_{el-ph}(T) \quad (10)$$

where ν_{el-ph} and γ_{el-ph} are due to electron-phonon interaction.

For the low-pump fluence case of 14 μ J/cm^2 (data shown in Figs. 5 (c) and (d)), the contribution of electron-phonon coupling is negligible and the temperature dependence arises predominantly from anharmonic interactions. Thus, by subtracting the values of $\nu_{ph}(T)$ and $\gamma_{ph}(T)$ shown in Figs. 5 (d) and 5 (c) from the corresponding values shown in Figs. 6 (a) and 6 (b), we obtain only the electron-phonon contribution to the phonon parameters (shown in Figs. 6 (c) and 6 (d)) at different carrier density levels. The solid lines in Fig. 6 (c) are fit to $\Delta\nu_{el-ph}(T) = \Delta\nu_{el-ph}(0) + A(N)T$, where the slope A is a function of photoexcited carrier density N. It can be seen that both $\Delta\nu_{el-ph}$ and $\Delta\gamma_{el-ph}$ strongly depend on the carrier density N. On the other hand, $\Delta\gamma_{el-ph}$ is weakly dependent on T. More theoretical understanding is needed to explain the trends seen in Fig. 6 (c) and (d).

V. CONCLUSIONS

Time-resolved reflectivity measurements of tellurium have been performed over a wide range of temperatures and photoexcited carrier densities. The relaxation time associated with the carrier diffusion increases with the pump fluence which is quantitatively understood based on a diffusion model. The temperature dependence of carrier relaxation time, τ_{el}, is observed to be anomalous. The oscillatory part of the time-resolved differential reflectivity shows highly chirped A_1 phonons excited at high carrier densities and the chirping is found to be largest at the lowest temperature where the carrier diffusion time and the strength of photoexcited carrier density are maximum. Apart from the chirping seen in phonons, the lattice displacements associated with them is estimated to be very high (e.g $\sim$ 0.24 Å at 3K). Another important result is the observation of increased softening of A_1 mode with the pump fluence at 3K (-0.16 THz/mJ-cm^{-2}) compared to 296K (-0.08 THz/mJ-cm^{-2}) consistent with the increased photoexcited carriers at low temperatures. Using low pump fluence transient reflectivity experiments, the effects of phonon anharmonicity and the contribution of electron-phonon interaction to the phonon frequencies and linewidths

at high pump fluence were separated. The temperature and photoexcited carrier density dependences of electron-phonon contribution to the mode frequency and linewidth needs to be understood theoretically.

ACKNOWLEDGEMENTS

AKS acknowledges the financial support from Department of Science and Technology of India. SK acknowledges University Grants Commission, India for senior research fellowship.

[1] A. Othonos, J. Appl. Phys. **83**, 1789 (1998).

[2] W. H. Knox, C. Hirlimann, D. A. B. Miller, J. Shah, D. S. Chemla, and C. V. Shank, Phys. Rev. Lett. **56**, 1191 (1986).

[3] J. L. Oudar, D. Hulin, A. Migus, A. Antonetti, and F. Alexandre, Phys. Rev. Lett. **55**, 2074 (1985).

[4] J. Shah, Ultrafast Spectroscopy of Semiconductors and Semiconductor Nanostructures (Springer Verlag, Berlin, 1996).

[5] L. Dhar, J. A. Rogers and K. A. Nelson, Chem. Rev. **94**, 157 (1994).

[6] H. J. Zeiger, J. Vidal, T. K. Cheng, E. P. Ippen, G. Dresselhaus, M. S. Dresselhaus, Phys. Rev. B. **45** 768 (1992).

[7] T. K. Cheng, M. S. Dresselhause, and E. P. Ippen, Appl. Phys. Lett. **62**, 1901 (1993).

[8] A. V. Kuznetsov and C. J. Stanton, Phys. Rev. Lett. **73**, 3243 (1994).

[9] G. A. Garrett, T. F. Albrecht, J. F. Whitaker, and R. Merlin, Phys. Rev. Lett. **77**, 3661 (1996).

[10] H. Dember, Phys. Z. **32**, 554 (1931).

[11] T. Dekorsy, H. Auer, C. Waschke, H. J. Bakker, H. G. Roskos, and H. Kurz, Phys. Rev. Lett. **74**, 738 (1995).

[12] T. Dekorsy, H. Auer, H. J. Bakker, H. G. Roskos, and H. Kurz, Phys. Rev. B **53**, 4005 (1996).

[13] S. Hunsche, K. Wienecke, T. Dekorsy, and H. Kurz, Phys. Rev. Lett. **75**, 1815 (1995).

[14] S. Hunsche,K. Wienecke, and H. Kurz, Appl. Phys. A, **62**, 499 (1996).

[15] P. Tangney, S. Fahy, Phys. Rev. B **65**, 054302 (2002).

[16] M. F. DeCamp, D. A. Reis, P. H. Bucksbaum, and R. Merlin, Phys. Rev. B **64**, 092301 (2001).

[17] M. Hase , M. Kitajima, S. I. Nakashima, and K. Mizoguchi, Phys. Rev. Lett. **88**, 067401 (2002).

[18] O. V. Misochko , M. Hase, K. Ishioka, and M. Kitajima, Phys. Rev. Lett. **92**, 197401 (2004).

[19] E. D. Murray, D. M. Fritz, J. K. Wahlstrand, S. Fahy, and D. A. Reis, Phys. Rev. B **72**, 060301 (2005).

[20] P. Stampfli and K. H. Bennemann, Phys. Rev. B **42**, 7163 (1990); **46**, 10686 (1992); **49**, 7299 (1994).

[21] A. S. Pine and G. Dresselhaus, Phys. Rev. B **4**, 356 (1971).

[22] S. Tutihasi, G. G. Roberts, R. C. Keezer, and R. E. Drews, Phys. Rev. **177**, 1143 (1969).

[23] G.C. Cho, W. K*ü*tt, and H. Kurz, Phys. Rev. Lett. **65**, 764(1990).

[24] M. F. Decamp, Ph.D Thesis, The University of Michigan, Ann Arbor (2002).

[25] T. Dekorsy, H. Auer, C. Waschke, H.J. Bakker, H.G. Roskos, H. Kurz, V. Wagner, and P. Grosse, Phys. Rev. Lett. **74**, 738 (1995).

[26] A. Q. Wu, X. Xu, and R. Venkatasubramanian, Appl. Phys. Lett. **92**, 011108 (2008).

[27] O. V. Misochko, K. Ishioka, M. Hase, and M. Kitajima, J. Phys.: Condens. Matter **18**, 10571 (2006).

[28] M. Balkanski, R. F. Wallis, E. Haro, Phys. Rev. B **28**, 1928 (1983).

[29] J. Menéndez and M. Cardona, Phys. Rev. B **29**, 2051 (1984).

[30] P. B. Allen, Phys. Rev. B **6**, 2577 (1972).

[31] M. Lazzeri, S. Piscanec, F. Mauri, A. C. Ferrari, and J. Robertson, Phys. Rev. B **73**, 155426 (2006).

FIGURE CAPTIONS:

Figure 1: (a) Normalized time-resolved reflectivity data (open circles) at T=3K at various pump fluences along with the fits (line) according to Eq. (2). (b) Corresponding FFT spectra of the oscillatory part of the data and fit. The vertical dashed line in (b) is the guide to the eye to appreciate the red shift of the phonon peak frequency.

Figure 2: (a) Normalized time-resolved reflectivity change ($\frac{\Delta R}{R}$) at T=3K at maximum pump fluence of 3.3 mJ/cm^2 along with the fit.(b) The FFT spectra of the oscillatory part of time domain part. Open circles represent the experimental data and thick line is the fit according to Eq. (2) with $\beta = 0.55$ and the grey line is with $\beta = 0$. (c) Carrier density dependence of strength of photoexcited carriers (A_{el}) and (d) photoexcited carrier relaxation time (τ_{el}) at different temperatures (T=3K (filled squares), 80K (filled circles), 160K (filled triangles), 296K (filled inverted triangles)). The fit, $A_{el} \sim N^p$ is shown in (c) with p =1.5 (3K), 1.6 (80K), 1 (160K and 296K). The lines in (d) are guide to the eye. (e) The temperature dependence of A_{el} and (f) τ_{el} at given carrier densities (C1 = 0.1×10^{21}cm^{-3}, C2 = 0.2×10^{21}cm^{-3}, C3 = 0.4×10^{21}cm^{-3}, C4 = 0.6×10^{21}cm^{-3}, C5 = 1.4×10^{21}cm^{-3}). The lines in (e) are the linear fits and in (f) are guide to the eye.

Figure 3: (A) Time domain data at 160K (open circles) and the corresponding fit (line) using the diffusion model (see text) at different fluences (a1)-(e1). (B) The diffusion time (filled stars), $\tau_d = \xi^2/D_a$ versus N (a2)-(d2) and T (e2)-(h2) (see text). Here D_a is the carrier diffusion coefficient and the solid lines are drawn as guide to the eye.

Figure 4: PCD dependance of phonon fit parameters: (a) phonon amplitude (B_{ph}), (b) phonon life time (τ_{ph}), (c) phonon chirping parameter (β) along with a fit $\sim N^\rho$ ($2.2 \leq \rho \geq 3.8$), and (d) the phonon frequency, ν_{ph} at two temperatures-296K and 3K. The inset of (d) shows the dependance of the slope (filled stars), y ($= \frac{1}{2\pi}\frac{\partial\Omega_0}{\partial N}$ THz cm^3) of the linear fits to the data as function of temperature (solid line is the linear fit). (e) The variation of the lattice displacement, U as a function of the sample temperature at different PCDs. The data in (a), (b) and (e) are connected by solid lines as a guide to the eye.

Figure 5: (a) Time domain data at lowest pump fluence of 14 μJ/cm^2 at 3K (open circles) along with fit to Eq. (1) (solid line). Inset is the FFT of the data and the fit. (a) Phonon amplitude, B_{ph} vs T, (c) phonon damping parameter, γ_{ph} vs T (d) the phonon frequency ν_{ph} vs T. The solid lines are based on cubic anharmonic fit (see text) and the open stars are the data.

Figure 6: Temperature dependence of (a) ν_{ph}, (b) γ_{ph}, (c) $\Delta\nu_{el-ph}$ and (d) $\Delta\gamma_{el-ph}$ at different carrier density levels. Legends C1-C5 corresponds to 0.1, 0.2, 0.4, 0.6 and 1.4 $\times$ 10^{21} cm^{-3}. The solid lines in (a), (b) and (c) are the linear fits. The dashed lines in (d) are the guide to the eye.

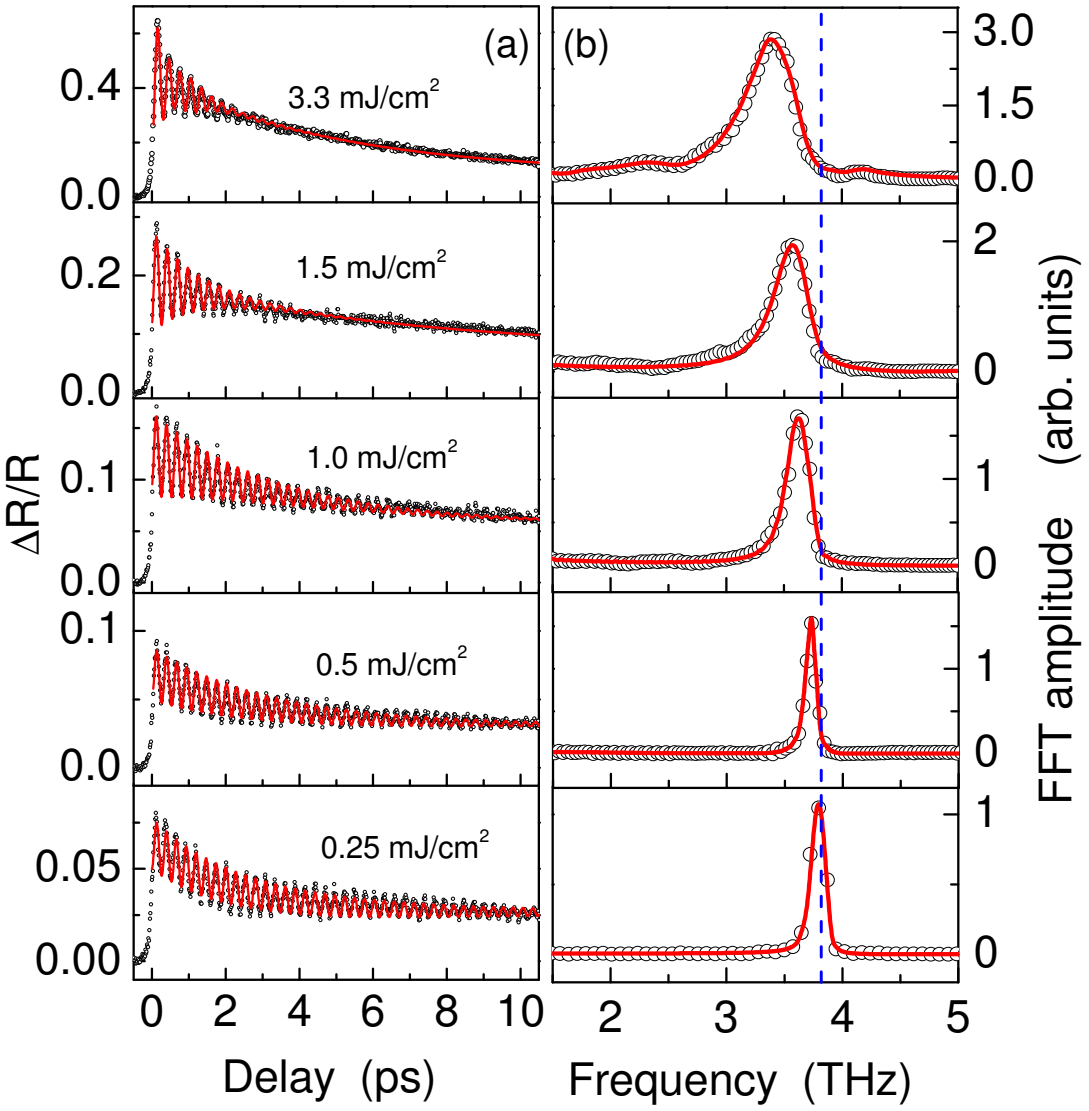

(a)
(b)
3.3 mJ/cm2
1.5 mJ/cm2
1.0 mJ/cm2
0.5 mJ/cm2
0.25 mJ/cm2
ΔR/R
Delay (ps)
Frequency (THz)
FFT amplitude (arb. units)

FIG. 1:

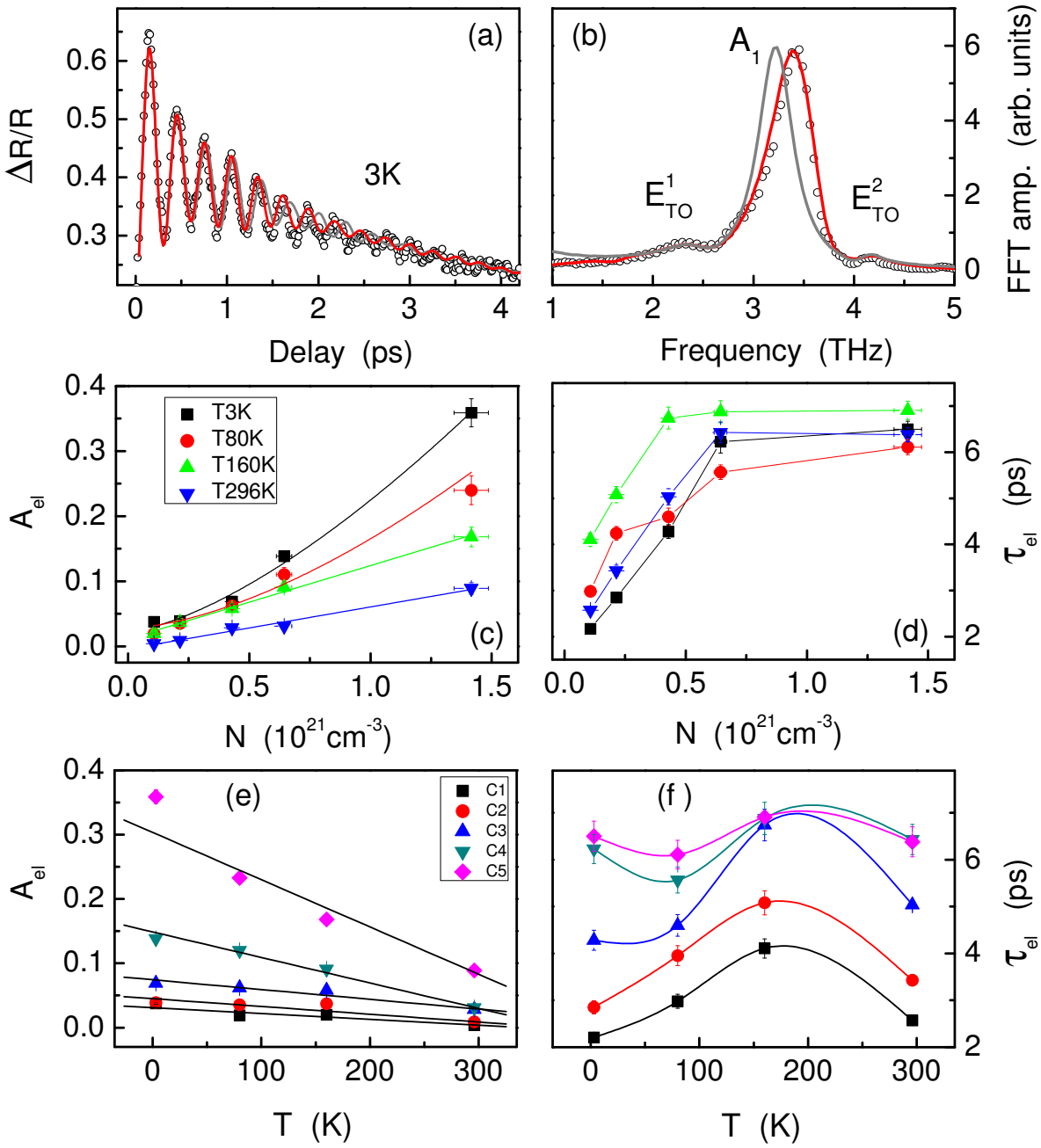
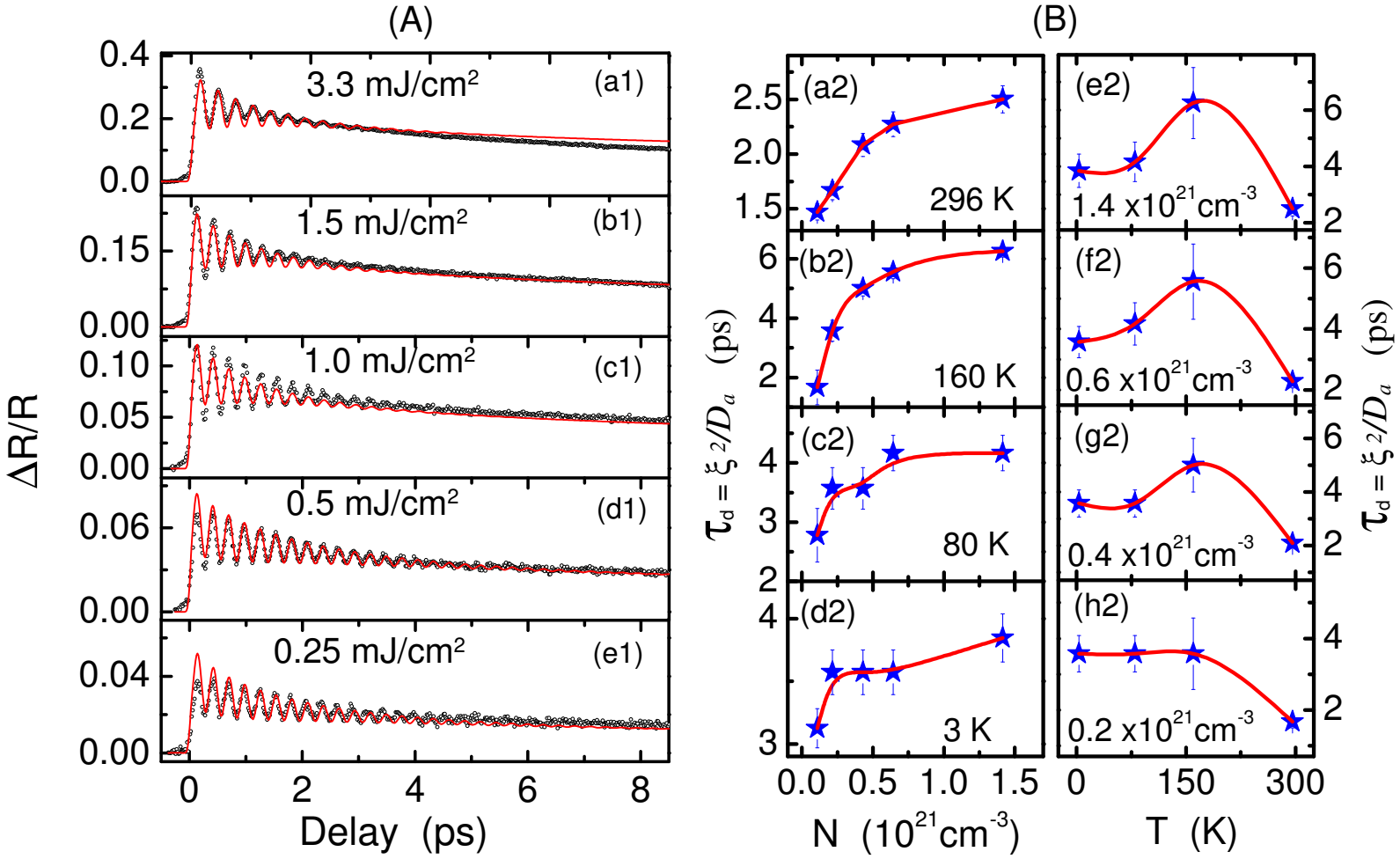

(a)
3K
ΔR/R
Delay (ps)
(b)
A1
E1TO
E2TO
FFT amp. (arb. units)
Frequency (THz)
T3K
T80K
T160K
T296K
(c)
Ael
N (10^21 cm^-3)
(d)
τel (ps)
(e)
C1
C2
C3
C4
C5
T (K)
(f)

FIG. 2:


(A)
(B)
3.3 mJ/cm²
(a1)
1.5 mJ/cm²
(b1)
1.0 mJ/cm²
(c1)
0.5 mJ/cm²
(d1)
0.25 mJ/cm²
(e1)
ΔR/R
Delay (ps)
(a2)
296 K
(b2)
160 K
(c2)
80 K
(d2)
3 K
(e2)
1.4 x10²¹cm⁻³
(f2)
0.6 x10²¹cm⁻³
(g2)
0.4 x10²¹cm⁻³
(h2)
0.2 x10²¹cm⁻³
τd = ξ²/Da (ps)
N (10²¹cm⁻³)
T (K)

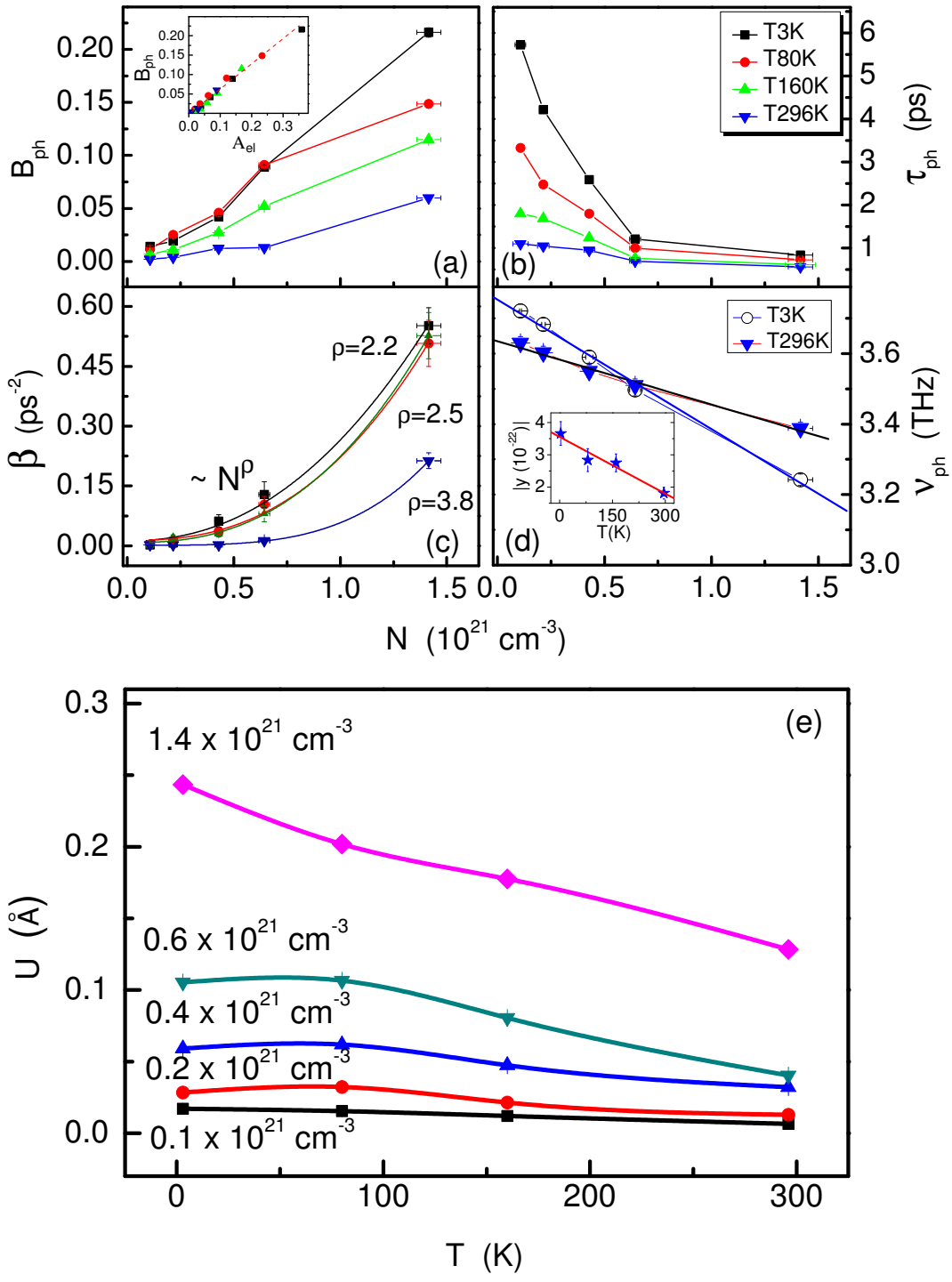

B_ph
A_el
(a)
T3K
T80K
T160K
T296K
τ_ph (ps)
(b)
β (ps^-2)
ρ=2.2
ρ=2.5
ρ=3.8
~ N^ρ
(c)
T3K
T296K
|y (10^-22)|
T(K)
(d)
ν_ph (THz)
N (10^21 cm^-3)
1.4 x 10^21 cm^-3
0.6 x 10^21 cm^-3
0.4 x 10^21 cm^-3
0.2 x 10^21 cm^-3
0.1 x 10^21 cm^-3
(e)
U (Å)
T (K)

FIG. 4:

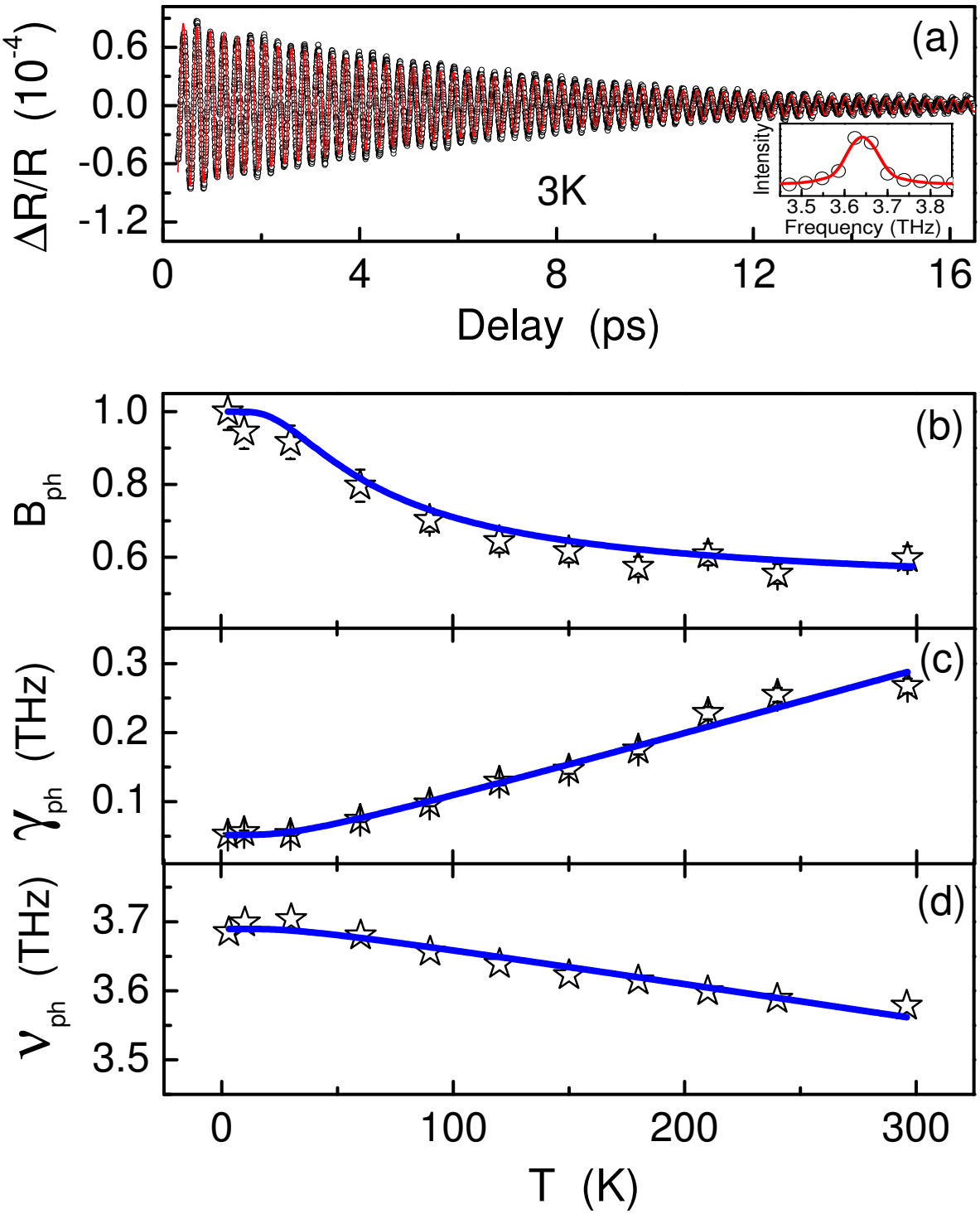

(a)
ΔR/R (10^-4)
0.6
0.0
-0.6
-1.2
3K
Intensity
3.5 3.6 3.7 3.8
Frequency (THz)
0
4
8
12
16
Delay (ps)
(b)
B_ph
1.0
0.8
0.6
(c)
γ_ph (THz)
0.3
0.2
0.1
(d)
ν_ph (THz)
3.7
3.6
3.5
0
100
200
300
T (K)

FIG. 5:

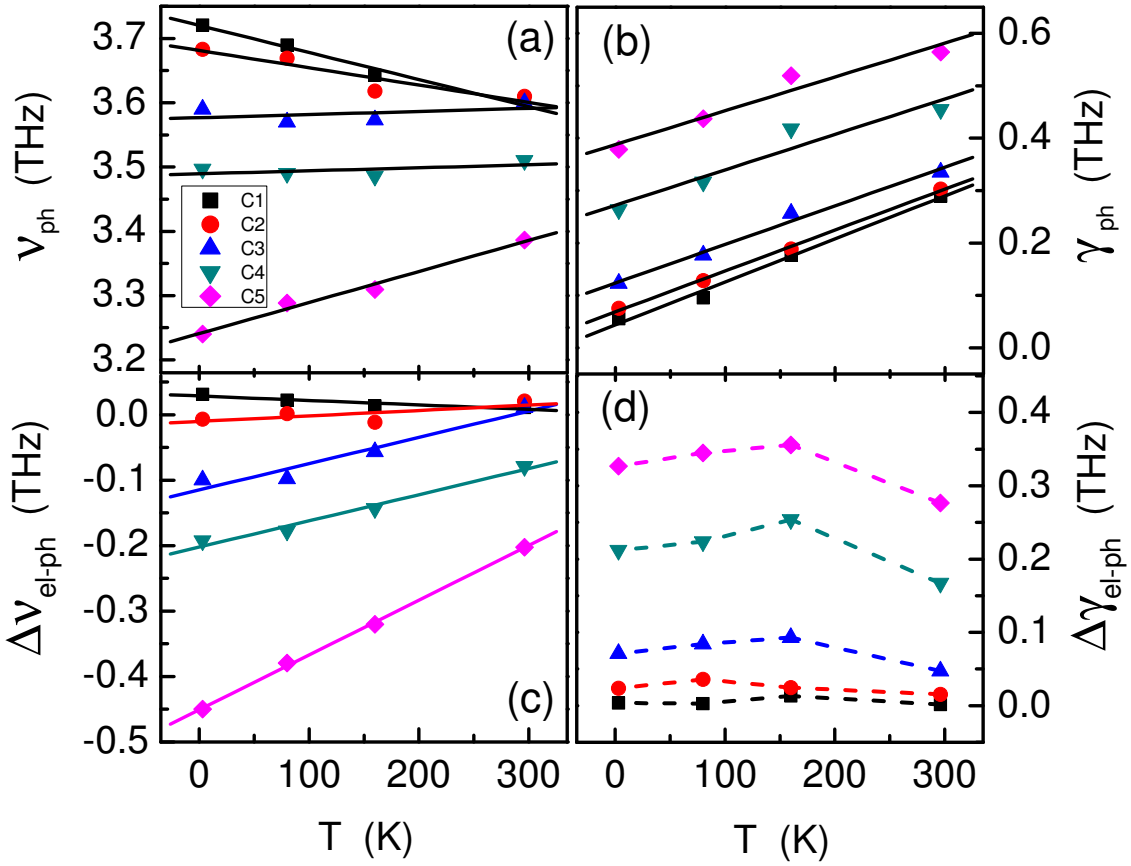

(a)
(b)
(c)
(d)
C1
C2
C3
C4
C5
ν_{ph} (THz)
γ_{ph} (THz)
$\Delta\nu_{el\text{-}ph}$ (THz)
$\Delta\gamma_{el\text{-}ph}$ (THz)
T (K)
T (K)

FIG. 6: